Environmentally influenced microstructurally small fatigue crack growth in cast magnesium

Ken Gall [a,*], Gerhard Biallas [b], Hans J. Maier [b], Mark F. Horstemeyer [c], David L. McDowell [d]

[a] *Department of Mechanical Engineering, University of Colorado, Boulder, CO 80309, USA*
[b] *Lehrstuhl für Werkstoffkunde (Materials Science), University of Paderborn, 33095 Paderborn, Germany*
[c] *Mechanical Engineering, Mississippi State University, Mississippi State, MS 39762, USA*
[d] *George Woodruff School of Mechanical Engineering, Georgia Institute of Technology, Atlanta, GA 30332, USA*

Abstract

We examine the growth of microstructurally small fatigue cracks in cast AM60B magnesium (Mg) cycled in a water vapor environment. The behavior and growth rates of the small cracks were measured in situ during cycling using a fatigue loading stage contained within an environmental scanning electron microscope (ESEM). We provide quantitative data describing the interaction of representative small fatigue cracks with microstructural features, along with the average growth rate data for approximately 20 different cracks. Small surface and corner cracks, with sizes ranging from 20 to 200 μm, are observed to interact strongly with the surface microstructure during growth. The small cracks preferentially propagate through the dendrite cells, and the particle laden interdendritic regions typically act as barriers to fatigue crack propagation. As the small cracks approach the interdendritic boundaries, measured growth rates decrease and the cracks sometimes becomes temporarily pinned at the boundary. Cracks smaller than 100 μm experience more significant disruptions in crack growth rates at interdendritic boundaries compared to the larger cracks that interact with the boundaries, but with less change in crack growth rates. Under nominally identical loading conditions, isolated microstructurally small cracks grow, on average, two orders of magnitude faster in a sample containing a higher fraction of porosity. The significantly higher crack growth rates in the more porous sample were attributed to local amplification of the nominal stress field in the vicinity of the microstructurally small cracks rather than explicit interactions between growing cracks and pores. Analogous to the wrought materials, the growth rate of microstructurally small cracks is observed to be significantly higher compared to long fatigue cracks at equivalent maximum cyclic stress intensity values.
© 2005 Elsevier B.V. All rights reserved.

Keywords: Cast magnesium; Fatigue; Small cracks; Environmental scanning electron microscopy; In situ fatigue

1. Introduction

Microstructurally small fatigue cracks have a size on the order of characteristic microstructural features in a material which, depending on the material, ranges from micrometers to hundreds of micrometers [1]. More important than absolute size is the notion that microstructurally small cracks interact strongly with the microstructure during growth and, thus, their behavior cannot be explicitly modeled without accounting for the effect of microstructural features. The growth behavior of microstructurally small fatigue cracks is often referred to as 'anomalous' since they typically grow faster than long fatigue cracks at the same applied stress intensity range, grow below the long fatigue crack growth threshold, and exhibit considerable growth rate variability [1–23]. However, as a recent review has pointed out [22], the growth behavior of long cracks at low stress intensity ranges, sometimes referred to as 'near threshold' growth behavior, is more of an anomaly for real materials and structures. In materials used in engineering applications, small fatigue cracks usually grow under the influence of the same applied stress spectra as large cracks. Consequently, the growth of microstructurally small fatigue cracks will dominate at 'near threshold' applied stress intensity ranges (small crack length, *a*) while long crack be-

* Corresponding author. Tel.: +1 303 735 2711; fax: +1 303 492 3498.
  E-mail address: kenneth.gall@colorado.edu (K. Gall).

havior is more relevant at relatively higher applied stress intensity ranges (large crack length, *a*).

For approximately 20 years, the study of microstructurally small cracks has been driven by the notion that 60–80% of a wrought material's high cycle fatigue life is typically spend forming and growing a crack to a size on the order of 100 μm [4]. More recently, the growth behavior of microstructurally small fatigue cracks has emerged as a critical research area driven by two basic needs. First, recent modeling efforts [24] have explicitly incorporated the growth behavior of microstructurally small fatigue cracks into multiscale life prediction methodologies for bulk materials, a future route for fatigue modeling suggested in [22]. Second, metal [25] and ceramic [26] materials experiencing fatigue in microsystems have spatial dimensions on the order of the material microstructure, so cracks may never leave the microstructural regime prior to the failure. In both the instances, it is critical to understand the interaction of small fatigue cracks with the material microstructure. In the present paper, we examine the growth behavior of microstructurally small fatigue cracks in cast magnesium (Mg) motivated by the development of a multi-scale fatigue model for this material.

Early work linking the growth behavior of small fatigue cracks to the material microstructure was performed on the wrought aluminum alloys [2,3,5,6,8]. These groundbreaking experimental studies revealed that microstructurally short fatigue cracks were often pinned at grain boundaries, resulting in a deceleration in the fatigue crack growth rate. A deceleration was not observed when the misorientation between adjacent grains was small, indicating that the unfavorable orientation of slip systems in the adjacent grain was the primary driver for the crack growth inhibition rather than the boundary itself [6]. Aside from the variable effect of grain boundaries on the small fatigue crack propagation, another key observation in early [2–10] and more recent [11–23] studies is the relatively high crack growth rates of microstructurally small fatigue cracks compared to the long cracks. The high crack growth rates in microstructually short fatigue cracks are often attributed to a lack of crack closure coupled with large-scale crack tip plasticity leading to relatively large crack tip opening and sliding displacements and high crack growth rates. From a fatigue life prediction point of view, the relatively high crack growth rate of microstructurally small cracks is critical since long fatigue crack growth data underpredicts growth rates and overestimates the life of a component. In fact, a conservative, "worst-case-scenario" life prediction methodology considers an upper bound on growth rate for microstructurally small cracks [22].

Compared to the studies in wrought materials, only a few researchers have examined the growth of microstructurally small fatigue cracks in lightweight cast materials [27–33]. The lack of small crack studies in lightweight castings can be partially attributed to the presence of porosity in such materials. If casting porosity exists on a scale greater than hundreds of micrometers, then the microstructurally short crack growth regime can be completely bypassed under typical high-cycle fatigue loading conditions. The fatigue behavior of such a material will be characterized by rapid crack formation at the largest pore followed by long fatigue crack growth until failure. However, in the absence of larger scale porosity, cracks in castings can nucleate at small isolated pores or second phase particles and subsequently experience a growth phase heavily influenced by the microstructural features. For example, in cast Mg, microstructurally small crack growth has been observed in high-pressure dye castings at sizes up to and less than a few hundred micrometers [32,33].

Advancements in casting technology for lightweight metals have helped to minimize porosity levels in high stress regions of castings and have thus prioritized the study of microstructurally short cracks with sizes on the order of 100 μm. Several studies [28,31] have shown that the average crack growth rate of small cracks in cast Al follows a power-law dependence on the applied stress and scales linearly with the crack length. Another discovery of previous studies on cast Al alloys is growth retardation caused by Si particles or microporosity at small crack sizes [27–30]. The dendrite walls, laden with Si particles, generally act as barriers to the propagation of microstructurally small fatigue cracks in cast Al, analogous to small crack blockage at grain boundaries in the wrought materials [6–10]. To the best of our knowledge, minimal work has been performed to characterize the growth of microstructurally small fatigue cracks in cast Mg.

Recent in situ studies on cast Mg [32] demonstrated a change in the fatigue growth behavior at a crack size of approximately 100 μm for a material cycled at a 90 MPa stress amplitude. In the cast Mg alloy of interest, 100 μm corresponds to approximately 6–10 times the average dendrite cell size [32]. Fatigue cracks smaller than 100 μm appeared sensitive to the microstructural features while cracks larger than 100 μm propagated closer to the Mode I manner with less microstructural interaction [32]. Another recent study on cast Mg [33] cycled at a 0.2% total strain amplitude (corresponding to a 90 MPa stress amplitude) showed a transition to long fatigue crack growth behavior at a crack size greater than 1000 μm, based on the fracture surface observations. The transition behavior was rationalized in terms of a critical maximum stress intensity factor necessary to create a forward plastic zone capable of engulfing a statistically significant fraction of the microstructure ahead of the fatigue crack. Given the crack size of 1000 μm and stress of 90 MPa, the critical maximum transition stress intensity value is calculated as approximately $K_{max} \sim 2.3 \, MPa\sqrt{m}$, which is consistent with the transition from the near threshold to Paris law long fatigue crack growth on da/dN–K_{max} crack growth curves [34]. The aforementioned work [32,33] has examined the qualitative aspects of fatigue crack formation and small crack growth in cast Mg in water vapor and vacuum environments. However, this previous work has not quantitatively characterized the growth rate of small cracks in Mg as explicitly influenced by the microstructural features.

Mayer et al. [34,35] have examined the fatigue behavior of cast Mg. The growth behavior of long fatigue cracks was

discovered to depend on the testing environment [34], consistent with the results in [32]. In particular, humid environments lowered the threshold for long fatigue crack propagation relative to a vacuum environment [34]. It was also discovered that the fatigue life of cast Mg scales closely with the size of the pore that forms a fatal fatigue crack [35]. From experimental observations of fracture surfaces, Mayer et al. [35] proposed a critical 'threshold' stress intensity factor required to propagate a small fatigue crack from a pore. The threshold stress intensity factor is based on the square root of the pore size and is lower than threshold values determined for long cracks in [34]. The results in [35] infer that microstructurally small cracks in cast Mg grow at rates below the traditional long fatigue crack growth threshold, as expected based on the previous studies in cast and wrought materials. Although the basic behavior of small cracks in cast Mg has been studied, work is needed to understand the explicit interaction of such cracks with various microstructural features. Such fundamental knowledge can be used for optimal alloy design and mechanism based multi-scale fatigue modeling.

In the present work, we examine the growth of microstructurally small fatigue cracks in cast Mg. We place primary emphasis on understanding the interaction of small cracks with the microstructural inhomogeneities, with secondary emphasis on studying the 'average' growth rates of small cracks in comparison to large cracks. Previous studies have successfully employed traditional in situ scanning electron microscopy (SEM) to monitor the growth and behavior of small fatigue cracks in various materials [36–38]. However, previous studies have shown that the testing environment considerably influences propagation behavior of both the small [32] and large [34] cracks in cast Mg. Consequently, in the present study, we employ an environmental SEM (ESEM) with an in situ fatigue loading stage to track the growth of the microstructurally small cracks in cast Mg. The ESEM is not limited by the high-vacuum constraints of traditional SEM and allows in situ imaging in a water vapor environment. Based on the previous observations of the fatigue crack growth in cast Mg [32,33], we focus our attention to the growth of small surface fatigue cracks with sizes in the range of 20–200 μm.

2. Materials and experimental methods

We examined a cast AM60B magnesium alloy of the nominal composition shown in Table 1. As described in more detail in related work [32], flat dog-bone shaped specimens were machined at various spatial locations from a 10 cm × 15 cm × 3 mm plate cast in a permanent mold by high-pressure dye casting. The test specimens had a 8 mm gage length and a 3 mm × 1 mm (approximately) gage cross section and were all tested with a polished surface finish optimized for the in situ studies. For the details on optimum surface preparation, see Ref. [32]. In our earlier study [32], small dimples were used in order to favor crack nucleation

Table 1
Chemical composition of AM60B Mg alloy

Mg	Balance
Al	5.5–6.5
Mn	0.25 min
Si	0.10 max
Zn	0.22 max
Fe	0.005 max
Cu	0.010 max
Ni	0.002 max
Other	0.003 max (total)

Values in weight percent.

in local regions in the gage length. This helped reduce the surface area that needed continuous inspection during testing. As the present study focuses on obtaining quantitative data on the interaction of small cracks with the microstructural inhomogeneities, artificial stress concentrations were not employed.

The in situ tests were performed using a screw-driven small-scale load frame fixed within an ESEM and completely reversed ($R = \sigma_{min}/\sigma_{max} = -1$) fatigue tests were performed at a displacement rate of 20 μm/s (approximate strain rate of 2×10^{-4} 1/s). Given this rather low maximum displacement rate, such a set-up is normally limited to conducting fatigue tests that employ stress amplitudes in the low-cycle fatigue regime. However, for the application of the alloy in mind, low stress amplitudes representative of the high-cycle fatigue regime are of prime interest. Consequently, a 135 MPa 'preloading' stress amplitude, $\sigma_a = (\sigma_{max} - \sigma_{min})/2$ was applied to the sample in order to accelerate the formation of cracks throughout the sample. Following precycling, the cyclic stress amplitude was reduced to 90 MPa which corresponds to about 60% of the 0.2% offset yield stress of AM60B [32], and this stress amplitude corresponds to a fatigue life of approximately 10^6 cycles when applied continuously. In order to minimize the effects of precycling on crack growth data, the cracks were not tracked directly after precycling at 135 MPa. Instead the growth of selected cracks was monitored during cycling at 90 MPa only after 90 cycles, i.e. actual data was acquired only after the cracks had escaped the influence of the larger plastic zone at the crack tips caused by precycling. In addition, we have used two different samples for the study; one from a high porosity region of the casting (Sample 1) and one from a low porosity region of the casting (Sample 2). On each sample, we tracked the growth behavior of several dozen isolated microstructurally small cracks.

The environmental effect on fatigue crack growth was captured by conducting the tests in water vapor at a pressure of 1.6×10^3 Pa (12 Torr). Water vapor at 12 Torr corresponds to 60% relative humidity at ambient room temperature conditions, which is close to the environmental conditions experienced by many actual components. Note that the SEM used is capable of capturing images in such an environment when operated at an accelerating voltage of 20 kV. It is well known, however, that the interaction of the electron beam with the environment can cause drastically different local gas fugacities

[39]. Moreover, environmental effects are usually most pronounced during plastic deformation [40,41]. Thus, the high voltage was always switched off during cycling. Thus, unless otherwise noted, all SEM imaging was performed during a hold period at one-half maximum tensile load to accentuate crack opening. The holds were conducted in displacement control and a minimal amount of stress relaxation (1% of max stress) occurred during the hold. In all the images presented here, the loading axis is vertical on the page. We also note that the image quality generally decreased during cycling in the water vapor environment. For this reason, we have provided a high quality image of the fatigue crack growth regions prior to crack advance. In subsequent in situ images, we have traced the dendrite cell boundaries using a grey overlay.

Crack growth rates, da/dN, were determined by the secant method, i.e. da/dN is set equal to $\Delta a / \Delta N$, where the crack growth increment, Δa, is calculated as the difference between an initial and final crack size for a specified number of cycles. In order to track the changes in crack growth rate with different microstructural features, the cycle interval between crack observations, ΔN, varied between 10 and 1000 cycles depending on the observed crack. The crack size at a given growth rate is given as the average of the initial and final crack size for a given ΔN step. The effective resolution of the SEM at the employed magnification (1000×) is approximately 200 nm, so the corresponding inherent crack growth rate resolution is 2×10^{-7} m/cycle. Based on the cycle observation intervals of 5 and 1000, the average crack growth rate resolutions are 4×10^{-8} and 2×10^{-10} m/cycle, respectively. In traditional long crack studies, averaging over consistently larger cycle intervals creates smaller average crack growth rate resolutions. In the present study, we are interested in the interaction of the fatigue crack over very small length scales, so we cannot average crack growth rates over large ΔN values without smearing out the effects we are investigating.

Two different crack types were observed during fatigue cycling; surface cracks with tips contained on one specimen surface, and corner cracks with individual tips on the adjacent surfaces. For the purposes of reporting crack length and calculating stress intensity factors [42,43], it is important to present the nomenclature used for the surface and corner cracks (Fig. 1). Based on post-mortem fractography of cracks in the present material, coupled with previous crack observations [42,43], it is assumed that the surface and corner cracks are semi-elliptical. The total crack length for surface cracks is defined by the long axis of an ellipse, $2a$, while the depth is defined by one-half of the short axis, b (Fig. 1). The crack length of the corner cracks is defined by one-half of the long axis of the ellipse, a, while the depth is defined by one-half of the short axis, b. The values of 'a' were directly measured in situ on the specimen surface, and for a few cracks final values of 'b' were determined post-mortem. Throughout, we report crack size as either "total crack length", $2a$, or "crack length", a, for surface cracks and "crack length", a, for corner cracks. The terms "mean crack length" or "mean total crack length"
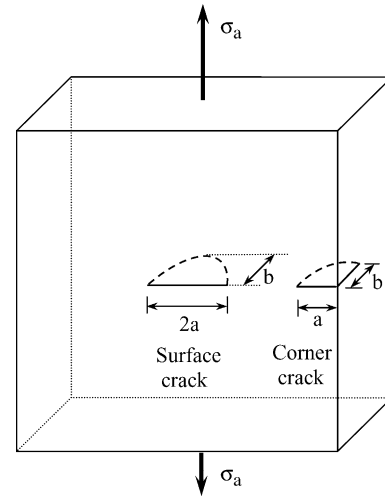

Fig. 1. Schematic defining surface and corner crack locations and geometries.

are used when crack length measurements are averaged over adjacent cycle intervals.

To calculate stress intensity values for the small cracks, we employed the square root area parameter for an elliptical crack [42]. The aspect ratio, a/b, of the elliptical surface and corner cracks was assumed constant at 1.25. The final stress intensity solution for an elliptical surface crack, embedded in a semi-infinite domain, with a total crack length of $2a$ is given as [42]:

$$K_{\max} = 0.65\sigma_{\max}\sqrt{\sqrt{\pi a\,(2\pi/5)}} \tag{1}$$

The stress intensity solution for an embedded elliptical corner crack with a crack length of a is given as [42,43]:

$$K_{\max} = 0.77\sigma_{\max}\sqrt{\sqrt{\pi a\,(2\pi/5)}} \tag{2}$$

The validity of Eqs. (1) and (2) depends on several assumptions that can break down for small fatigue cracks. In particular, it is necessary to have an isotropic medium with small scale crack tip yielding relative to the overall crack length. In the case of small fatigue cracks, the crack is embedded in an anisotropic medium and the isotropic elastic fracture mechanics solution only provides an average estimate of the crack tip stresses and strains. The plastic zone size for various crack lengths and applied stress values can be estimated using an Irwin type approach. For an applied maximum stress intensity factor of 1 MPa m$^{1/2}$ (in the typical range for the small cracks) and a yield strength of cast Mg of 150 MPa, the Irwin forward crack tip plastic zone size is on the order of 7 μm. The crack sizes in the present study range from 20 to 200 μm, so only the relatively smaller cracks would be in violation of small-scale yielding criteria. In either case, the stress intensity factor is the best tool for baseline normalization of the experimental results and comparison to long fatigue crack growth curves.

3. Small crack growth observations

Prior to presenting the experimental observations of small fatigue crack growth, we briefly discuss two issues related to the measurements. First, we recognize the measurements of fatigue crack growth were only performed on the specimen surface. In reality, the observed cracks all possessed a three-dimensional character. For example, one of the corner cracks observed in situ was contained in the final fracture path and the crack had a quarter-elliptical crack front profile. Consequently, although there may be a difference in the crack growth rate at the surface and farther into the material, we assert that the observed changes in the growth rates associated with various microstructural interactions mimic similar interactions seen along the crack periphery. Secondly, the three-dimensional nature of the crack can alter the interaction of the surface crack tip with inhomogeneities. For example, although an obstacle may have suppressed the surface crack growth rate, the crack front at other locations may or may not have encountered such a microstructural obstacle. Essentially, the progressing crack front in other locations may help to drive crack growth at a surface obstacle. This effect is insignificant when the crack is constrained to a few microstructural spacings in all the dimensions, and will become more pronounced when the crack front samples enough of the microstructure. In either case, despite the above issues, changes in the surface growth rates of small fatigue cracks were clearly linked to impingement upon microstructural features at the surface.

Although we have traced the crack growth behavior of approximately 20 cracks, detailed results from four representative cracks will be presented here. Cracks 1–3 are representative examples from Sample 1, which was extracted from a relatively high porosity region of the casting. Crack 4 is a representative example from Sample 2, which was extracted from a relatively low porosity region of the casting. Cracks 1 and 2 were corner cracks while Cracks 3 and 4 were surface cracks. Although Crack 4 began as a surface crack, it eventually became a corner crack by linking with another corner crack. We note that when two cracks linked, the stress intensity solution becomes strictly invalid but this does not impact very many cracks. Prior to presenting the in situ images, we briefly discuss the metallurgy of cast AM60 Mg as viewed in the SEM [32]. The most infrequent material phase is AlMnSi particles which are represented by raised bright white regions a few micrometers in size. The next darkest phase is the light grey β-$Al_{12}Mg_{17}$ particles. Their jagged shape and dispersion within the interdendritic regions most easily identifies the β-$Al_{12}Mg_{17}$ particles. The darkest and the most prominent phase is the hexagonal close packed (HCP) α-Mg which contains varying amounts of Al in solid solution. The contrast between the α and β phases in the SEM is relatively small under both backscatter and secondary imaging. This lack of contrast makes in situ imaging of crack growth behavior in cast Mg particularly challenging.

Figs. 2–13 present crack growth measurements and corresponding images of crack advance at critical intervals. The total crack lengths of the observed cracks vary from initial sizes in the range of 20–70 μm to final sizes in the range of 80–200 μm. In Figs. 4, 7, 9 and 11, we present (a) the crack length as a function of cycle number and (b) the crack growth rate as a function of mean crack length. We have shown both the raw and calculated data because both can provide insight into the cracks interaction with local microstructural features. Although the crack growth rate is reported near zero, the actual minimum resolvable crack growth rate at the small cycle intervals employed is discussed in Section 2. Determining precisely how fast the crack is propagating, as a function of cycle number, requires either averaging over a larger cycle number or higher resolution. Based on the current methodology, neither of these options are practical. From a practical point of view, crack growth rates near zero represent relative arrest of the crack for a finite cycle time.

Figs. 2–4 present crack growth data and images for Crack 1, a relatively large "microstructurally small" corner crack. Fig. 2 presents an overview image highlighting the microstructure prior to crack advance for Crack 1. Key locations for future crack tip positions are indicated in Fig. 2. Following Figs. 3 and 4, we observe the first arrest of Crack 1 at point B_1 when the crack tip reaches an interdendritic boundary. After passing the boundary at B_1, the crack growth rate increases in a fluctuating manner as it progresses halfway through the large dendrite cell. The drop in the average crack growth rate between points B_1 and C_1 was caused by the passage of the crack over the interdendritic porous region marked in Fig. 2. Crack 1 makes a brief arrest at point C_1 when it encounters a region in the center of the cell with AlMnSi particles (Fig. 2). After passing these particles, the growth rate of the crack increases through the dendrite cell until it reaches the interdendritic region at D_1 containing a β-$Al_{12}Mg_{17}$ particle (Fig. 2). A spike in the crack growth rate is experienced as
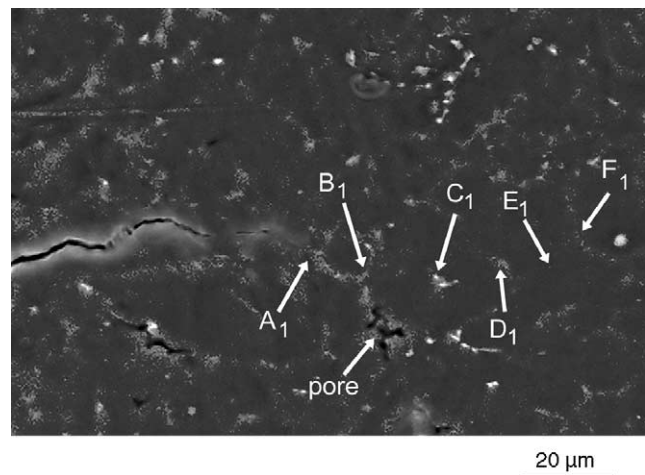

Fig. 2. Image highlighting the region of crack propagation for Crack 1 (visible on the left). The locations A_1–F_1 are points of interest where the crack intersects during subsequent growth.
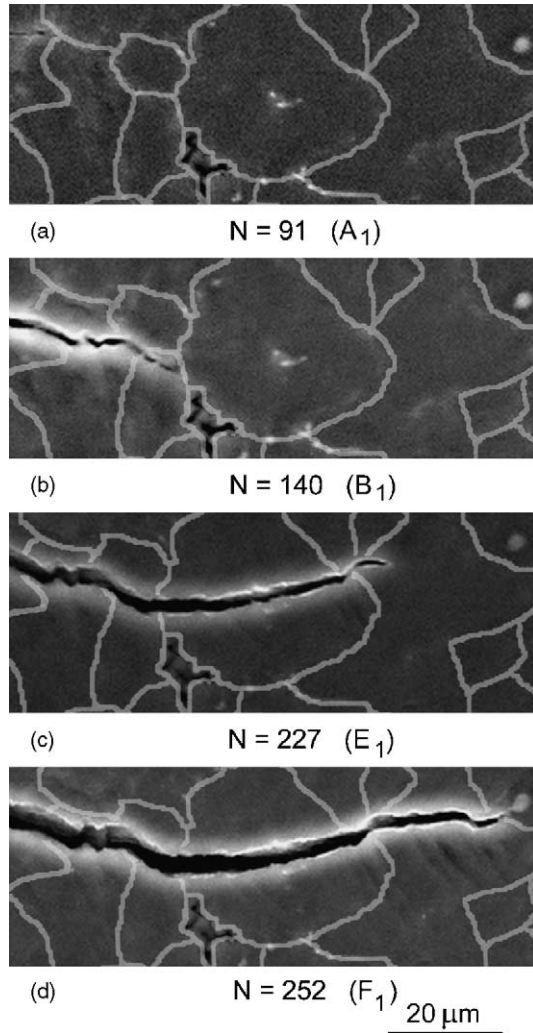
(a)   N = 91   (A$_1$)

(b)   N = 140   (B$_1$)

(c)   N = 227   (E$_1$)

(d)   N = 252   (F$_1$)   20 μm

Fig. 3. Selected in situ images during the growth of Crack 1 at locations (a) A$_1$, (b) B$_1$, (c) E$_1$ and (d) F$_1$. Approximate dendrite boundaries are highlighted by grey overlays.
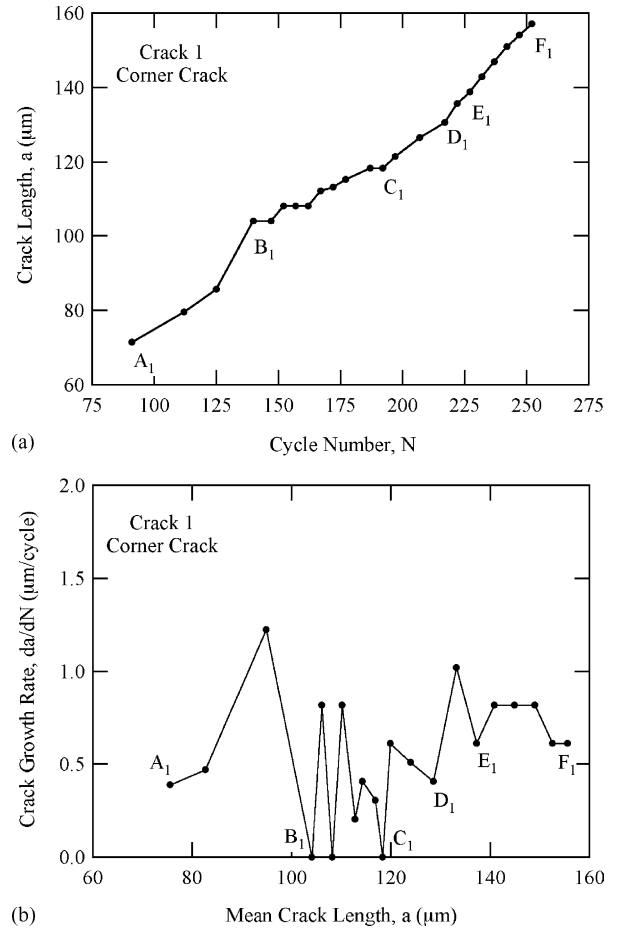

Fig. 4. Plots of (a) crack size as a function of cycle number and (b) crack growth rate as a function of mean crack length for Crack 1. The selected locations from Figs. 2 and 3 are shown at appropriate crack sizes and cycle numbers.
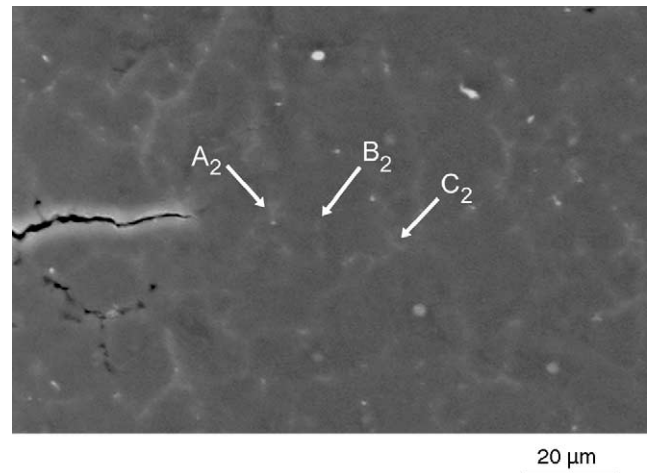
the crack passes this boundary and progresses to region E$_1$ (Fig. 3). Finally, Crack 1 grows steadily through another dendrite cell prior to slowing down near another interdendritic region, F$_1$ (Fig. 3).

Figs. 5–7 present crack growth data and images for Crack 2, a corner crack approximately half the total size of Crack 1. Although the surface growth behavior of Crack 1 was sensitive to the microstructural features at the surface, the relatively smaller Crack 2 demonstrated more severe changes in growth with respect to the surface microstructure. Fig. 5 presents an overview image highlighting the microstructure and key positions prior to crack advance for Crack 2. Figs. 6 and 7 show the growth patterns and respective growth data for Crack 2. Crack 2 makes three very distinct arrests at an interdendritic region (A$_2$), an Al rich region within the dendrite cell (B$_2$) and another interdendritic region (C$_2$). The crack growth suppression at regions A$_2$ and C$_2$ were clearly associated with the passage of the small crack tip through the interdendritic regions. In both the instances, the

Fig. 5. Image highlighting the region of crack propagation for Crack 2 (visible on the left). The locations A$_2$–C$_2$ are points of interest where the crack intersects during subsequent growth.

(a)

(b)

Fig. 7. Plots of (a) crack size as a function of cycle number and (b) crack growth rate as a function of mean crack length for Crack 2. The selected locations from Figs. 5 and 6 are shown at appropriate crack sizes and cycle numbers.
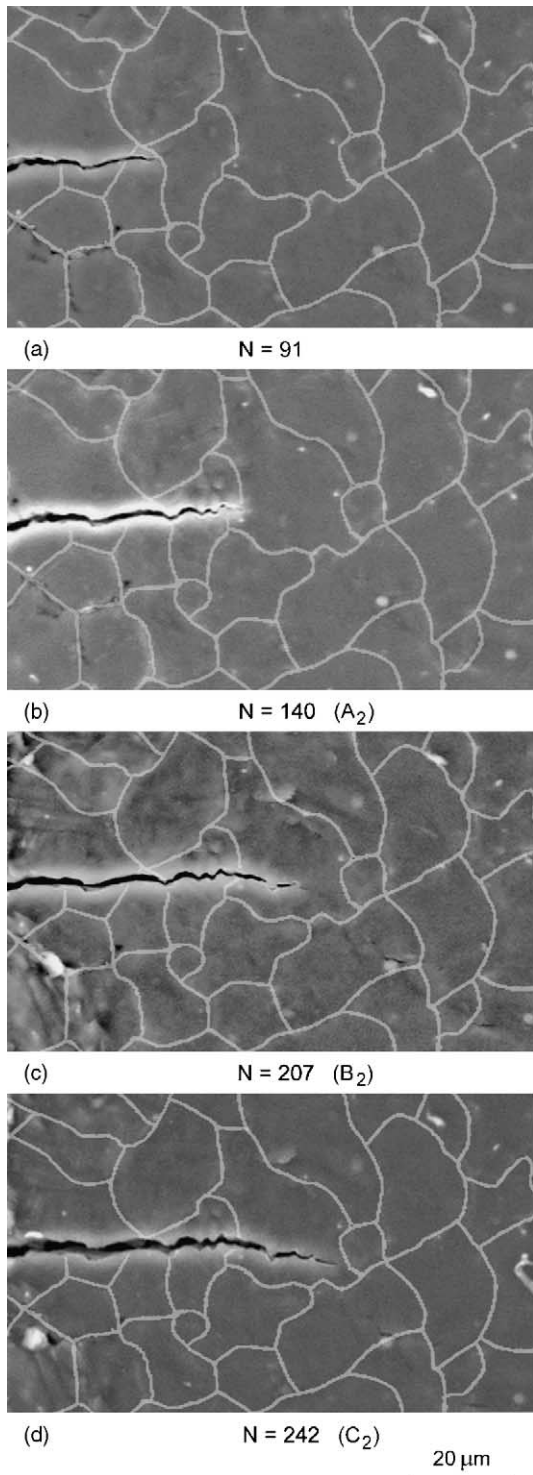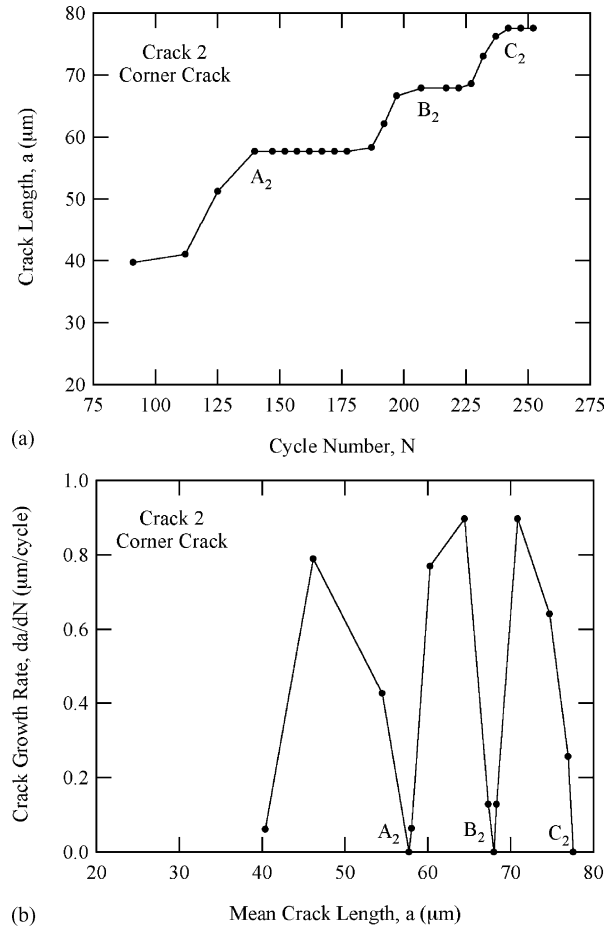

Fig. 6. Selected in situ images during the growth of Crack 2 at locations (a) 91 cycles, (b) A_2, (c) B_2 and (d) C_2. Approximate dendrite boundaries are highlighted by grey overlays.

crack encountered β-$Al_{12}Mg_{17}$ particles (faintly visible in Fig. 5). The inhibition of crack growth at region B_2 was linked to a material region containing a very high amount of Al in solid solution (7.1% versus 2.5% in surrounding areas).

Figs. 8 and 9 present images and crack growth data, respectively, for Crack 3, an extremely small surface crack growing in Specimen 1. Just after the formation, Crack 3 is contained within a dendrite cell. A dendrite boundary lies just to the right of Crack 3. During initial cycling (cycles 78–140), the growth rate of Crack 3 steadily decreases (Fig. 9). On the right, the crack growth is inhibited by a dendrite boundary while on the left, it grows through a region containing some second phase particles. Interestingly, upon further cycling, the right crack tip hardly progresses through the dendrite cell wall while the left crack tip moves across an open dendrite cell (Fig. 8c and d). As the left crack tip impinges on another dendrite cell wall, overall crack growth slows (Fig. 8d and 9). However, soon after this impingement, the right tip passes the right dendrite wall and overall crack growth rate increases (Figs. 8e and 9). The final images and crack growth data are presented for Crack 4 (Figs. 10 and 11). Crack 4 began as a small surface crack with a length on the order of the dendrite cell size. The growth rate of Crack 4 was much slower than the Cracks 1–3. Crack 4 grows somewhat steadily from cycles 2000 to 6000 (Figs. 10 and 11). Between cycles 6000
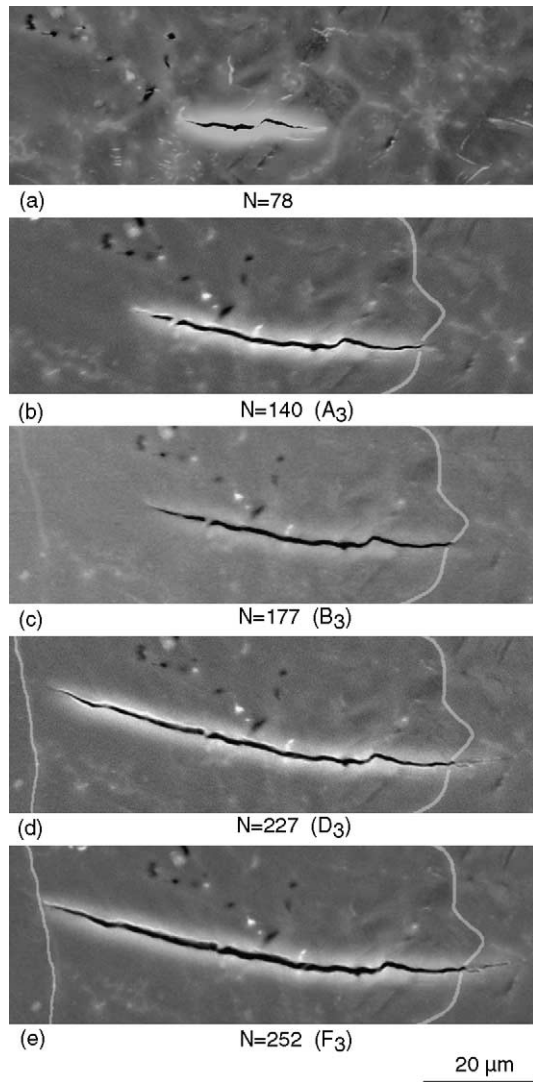
(a)

(b)

(c)

(d)

(e)

Fig. 8. Selected in situ images during the growth of Crack 3 at locations (a) 78 cycles, (b) A_3, (c) B_3, (d) D_3 and (e) F_3. Relevant dendrite boundaries are highlighted by grey overlays.
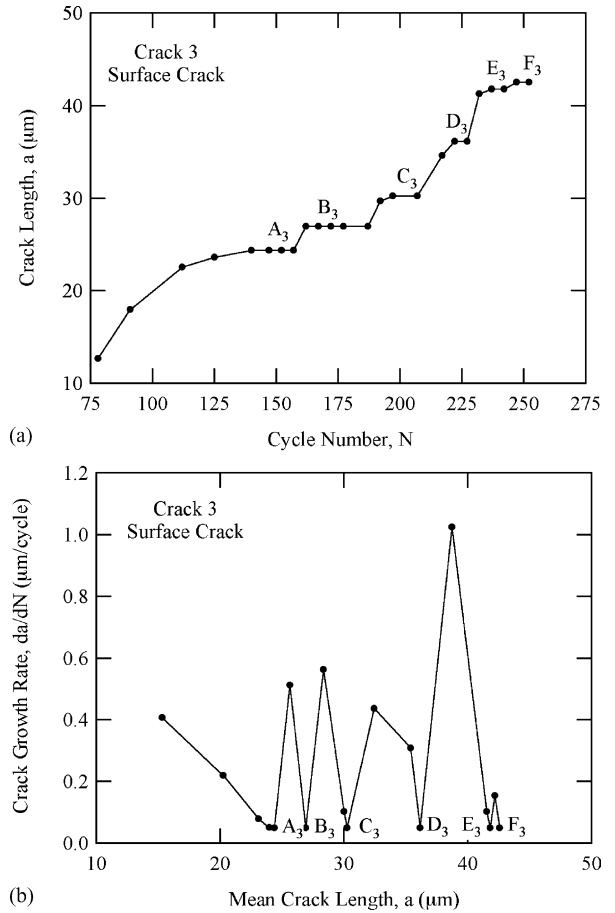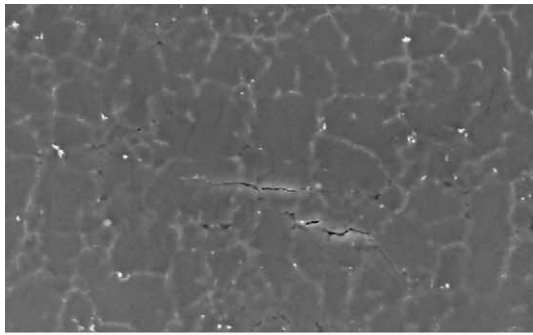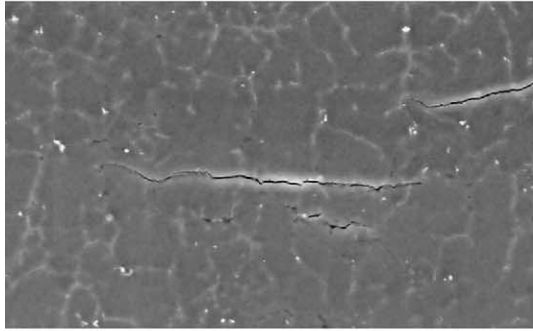

Fig. 9. Plots of (a) crack size as a function of cycle number and (b) crack growth rate as a function of mean crack length for Crack 3. The selected locations from Fig. 8 are shown at appropriate crack sizes and cycle numbers.

and 7000, Crack 4 links with a corner crack and thus experiences a discontinuous increase in crack length. Numerous observations were made on various cracks and the results presented here are representative of the majority of observations.

Of the four cracks presented here, only Crack 1 was contained on the fracture surface of Sample 1 after failure. A primary crack (initiated at a larger pore) linked with Crack 1 during final overload failure. Fig. 12 presents an image of the fracture surface of Crack 1 which formed and grew from the corner of the sample (upper left-hand corner). The crack front is quarter-elliptical in shape indicating similar crack growth rates at the surface of the sample and within the sample. Based on the equal progression of the crack at the surface and into the bulk, the damage observed at the surface was not exclusively a surface dominated effect. In addition, there was no observable evidence

of porosity or other defects at the nucleation site of Crack 1 (Fig. 12).

Fig. 13 provides a summary of the in situ small fatigue crack growth data from Samples 1 and 2. Long fatigue crack growth data for AM60hp [34] is included for reference. A few observations are noteworthy. First, the crack growth rates are considerable faster than the long fatigue crack growth data and growth occurs below the threshold stress intensity value (Fig. 13). These observations are consistent with the previous work on other cast and wrought alloys. Second, the scatter in crack growth rates is considerable within a given specimen, spanning two orders of magnitude for either specimen (Fig. 13). This scatter is consistent with the observed interactions of cracks with the microstructural features (Figs. 2–11). Finally, the crack growth rates of small cracks in Specimen 1 were consistently faster than crack growth rates in Specimen 2 (Fig. 13). In fact, the scatter in growth rates, considering data from both Specimens 1 and 2 covers approximately four orders of magnitude. The vast and systematic difference in growth rates between the two specimens was an unexpected observation.
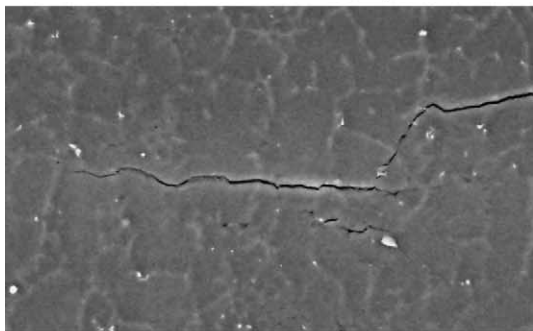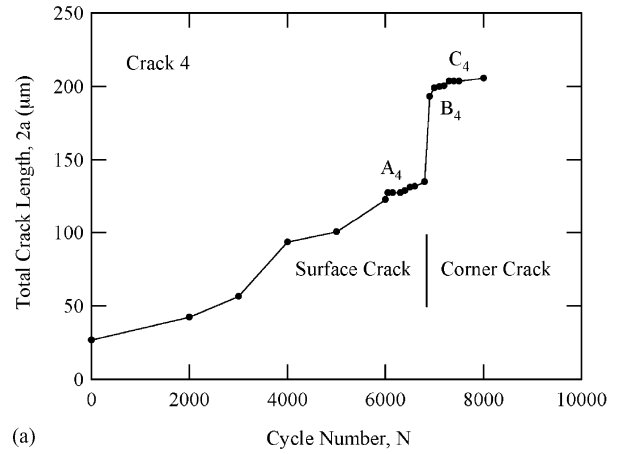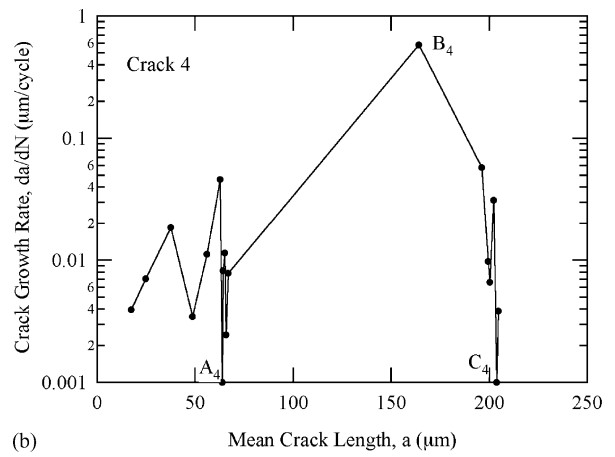
(a) N = 2000

(b) N = 6000 (A₄)
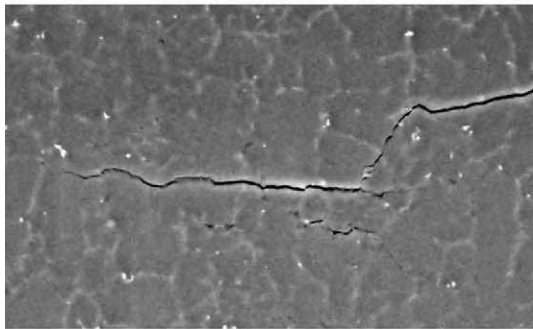
(c) N = 7000 (B₄)

(d) N = 7500 (C₄)

50 μm

Fig. 10. Selected in situ images during the growth of Crack 4 at locations (a) 2000 cycles, (b) A₄, (c) B₄, and (d) C₄.

Fig. 11. Plots of (a) crack size as a function of cycle number and (b) crack growth rate as a function of mean crack size for Crack 4. The selected locations from Fig. 10 are shown at appropriate crack sizes and cycle numbers.
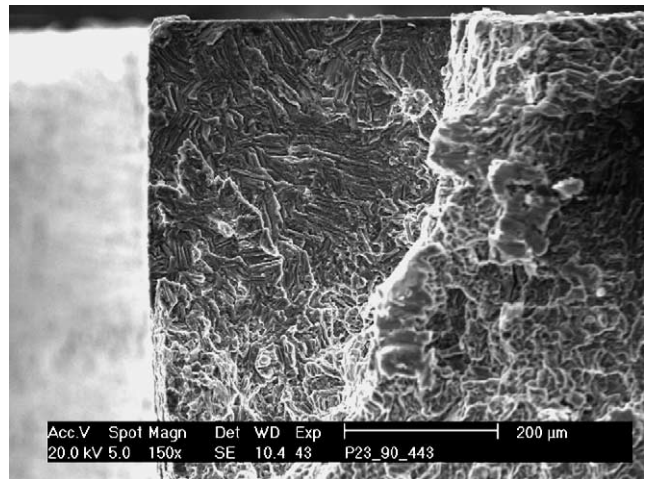

Fig. 12. Image of Crack 1 (corner crack in the upper left) on the fracture surface of Sample 1.
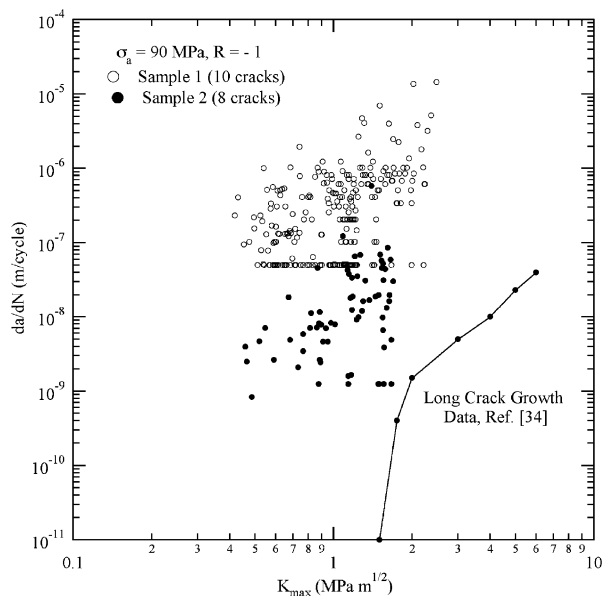
Fig. 13. Plot of da/dN vs. K_{max} for all cracks examined from Samples 1 and 2. The long fatigue crack growth data for AM60hp from [34] is included for reference.

4. Discussion

In order to fully optimize the performance of Mg castings in structural engineering applications, it is critical to understand the operant fatigue mechanisms. Moreover, a recent review [44] has re-emphasized the importance of understanding the fatigue behavior of cast Mg under the influence of environment. As casting technologies continually decrease porosity levels in high stress regions of castings, it becomes increasingly important to focus on the earlier stages of fatigue life such as fatigue crack formation and microstructurally small crack growth. In the present study, we have focused on understanding the growth of microstructurally small fatigue cracks in cast Mg cycled in a water vapor environment. The results provide a foundation for the explicit micromechanical modeling of microstructurally small fatigue crack growth [45] and ensuing multi-scale fatigue life modeling of cast magnesium.

Consistent with the qualitative observations in the previous work [32], we observe that microstructurally small fatigue cracks in cast Mg propagate preferentially inside the dendrite cells. The interdendritic regions contain second phase intermetallic particles and higher concentrations of Al in solid solution [32,33]. The hard particles and stronger matrix phase generally limit crack tip plasticity and opening and, thus, restrict fatigue crack growth. Crack 2 provides a very good example of the effect of interdendritic boundaries on fatigue crack growth (Figs. 5–7). At points A_2 and C_2, the crack becomes pinned at β intermetallic particles (faintly visible in Fig. 5). It is also interesting that the crack becomes pinned at region B_2 where the matrix contains a high concentration of Al in solid solution. Crack 3 also provides a good example of crack tip pinning at the interdendritic region. In particular, the

right crack tip (Fig. 8) becomes pinned on a boundary as the left tip propagates freely into the dendrite matrix. Once the left tip of Crack 3 begins to approach a boundary (Fig. 8), the right tip breaks free of the interdendritic boundary. We note that in the previous work [32], we observed small cracks to sometimes move preferentially across interdendritic regions. However, these observations were less frequent in the previous work and were also rare in the present study. The propagation of small cracks through interdendritic regions typically only occurs in the presence of interdendritic microporosity, a properly aligned (Mode I) boundary, or interdendritic damage due to plastic strain incompatibility between the adjacent dendrite cells. The latter mechanism is more prevalent during the high-stress, low-cycle fatigue of cast Mg where slip occurs within many dendrite cells [46].

Qualitatively, cracks smaller and larger than 100 μm interacted observably with the microstructure. However, from a quantitative crack growth rate standpoint, the boundaries had a much stronger effect on smaller cracks. For example, Cracks 1 and 2 differ in size by approximately a factor of two. Although Cracks 1 and 2 both show arrest points in Figs. 4a and 7a, respectively, Crack 2 spends many more cycles pinned at the boundary (Fig. 7a). This point is critical because it implies that even if a crack is noticeably interacting with the microstructure, the quantitative effect on overall propagation rate may be small. At this point, it is important to mention that the crack growth rate curves as a function of crack length can be misleading since a pinned crack will not experience a change in crack length. Even though locations A_2–C_2 correspond to arrest points for Crack 2, the arrest time is only marked by a single point (Fig. 7b). For this reason, we have included plots of crack length versus cycle number (Fig. 7a) which more clearly highlights the various crack arrest periods. The influence of crack length on the effectiveness of a hard second phase barrier has been examined using a micromechanical finite element model [45]. The results in [45] demonstrate that in cast Al, longer cracks have relatively larger crack tip plastic zones and crack tip opening displacements that are less affected by the presence of distributed hard inhomogeneties.

Fig. 13 provides a comprehensive synopsis of the small fatigue crack growth data for all of the cracks observed in the two different specimens. We have only used the stress intensity value with the caveat that it represents a good comparative tool even though it may not accurately describe the crack tip stress and strain fields for small cracks as discussed in Section 2. The long fatigue crack growth data [34] shows a near threshold transition close to a K_{max} value of $2 \, \text{MPa} \, \text{m}^{1/2}$. This transition stress intensity value also corresponds closely to the transition stress intensity $K_{max} = 2.3 \, \text{MPa} \, \text{m}^{1/2}$ where the fracture surface roughness significantly increases and the crack begins to preferentially travel almost exclusively through the interdendritic regions [33]. At the stress intensity values below $2.3 \, \text{MPa} \, \text{m}^{1/2}$, the fracture surface observations implied that the crack favored propagation through the dendrite cells [33]. The data in Fig. 13 represent cracks

with evolving lengths spanning 20–550 μm and corresponding maximum stress intensity values ranging from 0.4 to 2.5 MPa m$^{1/2}$. The cracks used for the representative observations in Figs. 2–12 were all smaller than 260 μm; thus, their maximum applied stress intensity value was always well below 2.3 MPa m$^{1/2}$. Since the cracks observed in Figs. 2–12 grew primarily through the dendrite cells, the present observations are consistent with the fracture surface observations inferring crack growth through the dendrite cells below a maximum stress intensity of 2.3 MPa m$^{1/2}$.

From a more quantitative perspective, a striking difference is seen in the crack growth behavior of Sample 1 (high porosity) and Sample 2 (low porosity). Samples 1 and 2 both show the signature behavior for microstructurally small cracks; relatively faster fatigue crack propagation rates compared to long cracks at equivalent stress intensity values, and propagation below the long fatigue crack growth threshold. However, the growth rates of Sample 1 are, on average, approximately two orders of magnitude faster than the growth rates in Sample 2. Recall that the samples were subjected to identical loading and imaging conditions with the only difference being the region of the casting they were extracted from. After fatigue failure, the fracture surface of both the samples revealed a very significant, but expected, difference; Sample 1 contained a significant fraction of porosity on the fracture surface while Sample 2 did not. However, it is very important to recognize that most of the observed microstructurally small cracks in both Samples 1 and 2 did not explicitly intersect pores. In fact, particularly in Sample 1, cracks with growth patterns clearly influenced by porosity were avoided.

Although the consistently higher crack growth rates of Sample 1 are not an artifact of explicit interaction with pores, the porosity must have an "indirect" influence on the growth rates (Fig. 13). This concept can be best appreciated by considering Crack 1. Although porosity was not discovered on the fracture surface created by Crack 1 (Fig. 12), Crack 1 did grow above a porous region (Fig. 2). The results in Fig. 13 can be explained if we assume the nominal stress field is locally amplified by the presence of widespread porosity. Amplification of the local stress field, such as would occur near a notch, leads to higher crack tip driving forces and enhanced growth rates. Although this is only a hypothesis at this point, previous small crack growth observations on cast aluminium have shown that an increase in the applied stress from $0.65\sigma_y$ to $0.91\sigma_y$ leads to an increase in small fatigue crack growth rates by nearly two orders of magnitude [31]. Interestingly, on a da/dN–ΔK curve, the increase in growth rates is represented by a nearly perfect vertical shift with an increase in the applied stress [31]. The two samples in the present study also demonstrated a very strong vertical shift in crack growth data (Fig. 13). Please note that a 50% change in the applied stress only results in a small horizontal shift in the data fields in Fig. 13 on the log scale. In summary, based on our observations, coupled with previous results on the effect of the applied stress on the growth rate of small cracks, we believe the porosity generally enhances the nominal stress

field experienced by the microstructurally small cracks. This enhancement leads to relatively higher small crack growth rates in the higher porosity sample even in the absence of explicit interaction between the small cracks and pores.

In closing, we mention future work is needed to fully understand the growth of microstructurally small fatigue cracks in cast Mg. In particular, the present results have shown that interdendritic regions serve as obstacles for small fatigue cracks. However, unlike most wrought materials, the interdendritic regions contain both hard particles as obstacles to fatigue crack propagation in addition to possible crystallographic misorientations. At present, the relative influence of dendrite cell misorientation (which may be critical in this hcp material) versus the second phase particles and hardened matrix material at the boundary is unclear. In addition, further work is needed to systematically quantify the effects of crack length, porosity and nominal stress on crack propagation rates uncovered in the present work.

5. Conclusions

(1) Microstructurally small fatigue cracks in cast Mg preferentially propagate through the dendrite cells. When the propagating fatigue cracks encounter a particle laden interdendritic region, fatigue crack growth rates usually demonstrate a measurable decrease. In some instances, the crack even experiences temporary pinning at the interdendritic region.

(2) Cracks smaller than 100 μm are more strongly influenced by interdendritic regions compared to relatively larger cracks. Cracks less than 100 μm often show complete arrest at interdendritic regions for a finite number of cycles. Cracks larger than 100 μm are noticeably perturbed at the interdendritic regions, however, their growth rate is only affected over a very small cycle interval.

(3) The measured growth rate of microstructurally small fatigue cracks in cast Mg is significantly higher than long fatigue crack growth rates at equivalent maximum cyclic stress intensity values. Furthermore, microstructurally small cracks contained within a high porosity specimen were consistently observed to grow faster than small cracks in a low porosity specimen. Since the isolated cracks in both the specimens were not observed to explicitly interact with any pores, we hypothesized that the higher growth rates are attributed to a local amplification of the nominal stress amplitude due to the presence of porosity. This conjecture needs future research for proof.

References

[1] R.O. Ritchie, J. Lankford, Small Fatigue Cracks, The Metallurgical Society Inc., Warrendale, PA, 1986, pp. 1–5.

[2] S. Pearson, Eng. Fract. Mech. 7 (2) (1975) 235–247.

[3] W.L. Morris, Met. Trans. A 8A (1977) 589–596.

[4] J. Schijve, Eng. Fract. Mech. 11 (1979) 167–221.

[5] W.L. Morris, Met. Trans. A 11A (1980) 1117–1123.

[6] J. Lankford, Fatigue Fract. Eng. Mater. Struct. 5 (3) (1982) 233–248.

[7] K.S. Chan, J. Lankford, Scr. Metall. 17 (1983) 529–532.

[8] A.K. Zurek, M.R. James, W.L. Morris, Met. Trans. A 14A (1983) 1697–1705.

[9] J. Lankford, D. Davidson, K.S. Chan, Metall. Trans. A 4 (1984) 1459–1488.

[10] E.R. de los Rios, H.J. Mohamed, K.J. Miller, Fatigue Fract. Eng. Mater. Struct. 8 (1) (1985) 49–63.

[11] R.O. Ritchie, J. Lankford (Eds.), Small Fatigue Cracks, The Metallurgical Society, Warrendale, PA, 1986.

[12] K.J. Miller, E.R. de los Rios (Eds.), The Behavior of Short Fatigue Cracks, European Group on Fracture, Mechanical Engineering Publications Ltd., London, UK, 1986, Publication No. 1.

[13] B.N. Leis, A.T. Hopper, J. Ahmad, D. Broek, M.F. Kanninen, Eng. Fract. Mech. 23 (5) (1986) 883–898.

[14] K. Tanaka, Y. Akiniwa, Y. Nakai, R.P. Wei, Eng. Fract. Mech. 24 (6) (1986) 803–819.

[15] K.J. Miller, Fatigue Fract. Eng. Mater. Struct. 10 (2) (1987) 93–113.

[16] A. Navarro, E.R. de los Rios, Fatigue Fract. Eng. Mater. Struct. 10 (2) (1987) 169–186.

[17] A. Plumtree, B.P.D. O'Conner, Fatigue Fract. Eng. Mater. Struct. 14 (2/3) (1991) 171–184.

[18] J.C. Newman, Fatigue Fract. Eng. Mater. Struct. 17 (4) (1994) 429–439.

[19] D.L. McDowell, Int. J. Fract. 80 (1996) 103–145.

[20] K. Gall, H. Sehitoglu, Y.F.E.M. Kadioglu, Acta Mater. 44 (1996) 3955–3965.

[21] K. Hussain, Eng. Fract. Mech. 58 (4) (1997) 327–354.

[22] J.C. Newman, Prog. Aerosol Sci. 34 (5-6) (1998) 347–390.

[23] A.J. McEvily, Mater. Sci. Res. Int. 4 (1) (1998) 3–11.

[24] D.L. McDowell, K. Gall, M.F. Horstemeyer, J. Fan, Eng. Fract. Mech. 70 (2003) 49–80.

[25] K. Gall, M. Hulse, M.L. Dunn, D. Finch, S.M. George, B.A. Corff, J. Mater. Res. 18 (7) (2003) 1575–1587.

[26] C.L. Muhlstein, E.A. Stach, R.O. Ritchie, Acta Mater. 50 (14) (2002) 3579–3595.

[27] A. Plumtree, S. Schafer, in: K.J. Miller, E.R. de los Rios (Eds.), The Behavior of Short Fatigue Cracks, EFG Publication 1, Mechanical Engineering Publications, London, 1986, pp. 215–227.

[28] K. Shiozawa, Y. Tohda, S.-M. Sun, Fatigue Fract. Eng. Mater. Struct. 20 (2) (1997) 237–247.

[29] K. Gall, N. Yang, M.F. Horstemeyer, D.L. McDowell, J. Fan, Metall. Trans. A 30 (1999) 3079–3088.

[30] S. Gungor, L. Edwards, Fatigue Fract. Eng. Mater. Struct. 16 (4) (1993) 391–403.

[31] M.J. Caton, J.W. Jones, J.E. Allison, Mater. Sci. Eng. A 314 (1-2) (2001) 81–85.

[32] K. Gall, G. Biallas, H.J. Maier, P. Gullet, M.F. Horstemeyer, D.L. McDowell, J. Fan, Int. J. Fatigue 26 (1) (2003) 59–70.

[33] M.F. Horstemeyer, Y. Yang, K. Gall, D.L. McDowell, J. Fan, P. Gullett, Fatigue Fract. Eng. Mater. Struct. 25 (2002) 1045–1056.

[34] M. Papakyriacou, H. Mayer, U. Fuchs, S.E. Stanzl-Tschegg, R.P. Wei, Fatigue Fract. Eng. Mater. Struct. 25 (8–9) (2002) 795–804.

[35] H. Mayer, M. Papakyriacou, B. Zettl, S.E. Stanzl-Tschegg, Int. J. Fatigue 25 (3) (2003) 245–256.

[36] M.D. Halliday, P. Poole, P. Bowen, Fatigue Fract. Eng. Mater. Struct. 18 (6) (1995) 717–729.

[37] Y. Mutoh, T. Moriya, S.J. Zhu, Y. Mizuhara, Mater. Sci. Res. Int. 4 (1) (1998) 19–25.

[38] X.P. Zhang, C.H. Wang, L. Ye, Y.W. Mai, Fatigue Fract. Eng. Mater. Struct. 25 (2) (2002) 141–150.

[39] T. Tabata, H.K. Birnbaum, Scr. Metall. 17 (1983) 947–950.

[40] M. M-Reger, L. Rémy, Metall. Trans. A 19A (1988) 2259–2268.

[41] H.J. Maier, R.G. Teteruk, H.-J. Christ, Metall. Mater. Trans. A 31A (2000) 431–444.

[42] Y. Murakami, Eng. Fract. Mech. 22 (1985) 101–114.

[43] H. Noguchi, T. Yoshida, R.A. Smith, Int. J. Fract. 112 (2001) 163–181.

[44] C. Potzies, K.U. Kainer, Adv. Eng. Mater. 6 (2004) 281–289.

[45] J. Fan, D.L. McDowell, M.F. Horstemeyer, K. Gall, Eng. Fract. Mech. 68 (2001) 1687–1706.

[46] K. Gall, G. Biallas, H.J. Maier, P. Gullet, M.F. Horstemeyer, D.L. McDowell, Met. Mater. Trans. 35 (2004) 321–331.